PHYSICAL REVIEW B, VOLUME 64, 125206

Multiaxial channeling study of disorder accumulation and recovery in gold-irradiated $6H$-SiC

W. Jiang* and W. J. Weber
Pacific Northwest National Laboratory, P.O. Box 999, Richland, Washington 99352

(Received 3 May 2001; published 10 September 2001)

Single crystal $6H$-SiC has been irradiated 60° off normal with 2 MeV Au^{2+} ions at 300 K to fluences of 0.029, 0.058, and 0.12 ions/nm^2, which produced relatively low damage levels. The disorder profiles as a function of ion fluence on both the Si and C sublattices have been determined simultaneously *in situ* using Rutherford backscattering and nuclear reaction analysis with 0.94 MeV D^+ ions in channeling geometry along the $\langle 0001\rangle$, $\langle 1\bar{1}02\rangle$, and $\langle 10\bar{1}\bar{1}\rangle$ axes. Along the $\langle 0001\rangle$ axis at these low doses, similar levels of Si and C disorder are observed, and the damage accumulation is linear with dose. However, along $\langle 1\bar{1}02\rangle$ and $\langle 10\bar{1}\bar{1}\rangle$, the disorder accumulation is larger and increases sublinearly with dose. Furthermore, a higher level of C disorder than Si disorder is observed along the $\langle 1\bar{1}02\rangle$ and $\langle 10\bar{1}\bar{1}\rangle$ axes, which is consistent with a smaller threshold displacement energy on the C sublattice in SiC. The mean lattice displacement, perpendicular to each corresponding axis, ranges from 0.014 to 0.037 nm for this range of ion fluences. A steady accumulation of small displacements due to lattice stress is observed along the $\langle 10\bar{1}\bar{1}\rangle$ axis, and a detectable reduction of the lattice stress perpendicular to the $\langle 0001\rangle$ axis occurs at 0.12 Au^{2+}/nm^2. There is only a moderate recovery of disorder, produced at and below 0.058 Au^{2+}/nm^2, during thermal annealing at 570 K; more significant recovery is observed for 0.12 Au^{2+}/nm^2 along both the $\langle 0001\rangle$ and $\langle 1\bar{1}02\rangle$ axes.

DOI: 10.1103/PhysRevB.64.125206 PACS number(s): 61.80.Jh, 61.72.Cc, 61.82.Fk, 61.85.+p

I. INTRODUCTION

Significant research efforts have been devoted to the study of silicon carbide (SiC) polytypes in the past decade because of the excellent physical and chemical properties of SiC that make it a prominent candidate for the fabrication of high-temperature, high-power, and high-frequency microelectronic and optoelectronic devices.[1–3] Silicon carbide has also been proposed for potential nuclear applications that include the structural component in fusion reactors,[4] cladding material for gas-cooled fission reactors,[5] and an inert matrix for the transmutation of plutonium and other transuranics.[6] Extensive experimental investigations of irradiation-induced damage accumulation and recovery in SiC have been performed,[7–13] leading to improved understanding and models of damage accumulation processes.[14] In addition, molecular-dynamics (MD) simulations of damage production[15–19] and accumulation[20–22] processes are consistent with many experimental observations and are providing atomic-level insights into ion-irradiation effects in SiC.

Ion-channeling methods based on Rutherford backscattering spectrometry (RBS/C) are frequently employed in studies of SiC to quantitatively determine the depth profiles of disorder on the Si sublattice.[7,8,10,11,23–26] More recently, the authors have utilized both RBS/C and nuclear reaction analysis in channeling geometry (NRA/C) to profile damage accumulation on both the Si and C sublattices.[12,27] Most of the previous studies employing channeling methods have been carried out along only one major crystallographic axis; however, using only a single crystallographic direction, some types of defects may not be observed due to shadowing effects. Although angular scans around multiple axes have been applied in other materials to determine the site locations of some implanted species[28,29] and lattice displacements of host atoms,[30,31] there are few studies where the accumulation of irradiation-induced disorder in SiC has been determined by means of multiaxial channeling analysis. In one of the few multiaxial studies on SiC,[32] RBS/C results obtained along the $\langle 100\rangle$ and $\langle 011\rangle$ channeling directions in $3C$-SiC irradiated with Al^+ and Si^+ indicate a "preferential" disordering process on the Si sublattice along the $\langle 011\rangle$ direction, which is due to the uniaxial irradiation-induced lattice strain along the $\langle 100\rangle$ axis. This behavior was later confirmed in an investigation of damage accumulation in Ar^+-irradiated $3C$-SiC.[33] In another study, the accumulated disorder on the Si sublattice in $6H$-SiC, derived from *in situ* RBS/C along the $\langle 1\bar{1}02\rangle$ axis, was observed to increase more rapidly with dose than that determined *ex situ* along the $\langle 0001\rangle$ axis.[7,34] The different axial behavior in $6H$-SiC was attributed to either defect recovery at room temperature or enhanced dechanneling along the $\langle 1\bar{1}02\rangle$ direction due to the uniaxial strain along the $\langle 0001\rangle$. Similarly, there are very few, if any, multiaxial studies on thermal recovery of irradiation-induced disorder in SiC. Additional *in situ* studies of damage accumulation and recovery along multiple channeling directions are clearly needed to develop a better understanding of the nature and recovery of irradiation damage in SiC, not only on the Si sublattice but also on the C sublattice. The results of such a study on the accumulation and recovery of disorder on both the Si and C sublattices in Au^{2+}-irradiated $6H$-SiC using *in situ* multiaxial RBS/C and NRA/C methods are reported in the present paper.

II. CRYSTALLOGRAPHIC STRUCTURE OF $6H$-SiC

Silicon carbide is a covalently bonded compound that has about 200 existing polymorphs with the same basal plane but different stacking order. One of the most common polytypes of interest is $6H$-SiC, which has a hexagonal structure and consists of a six-layer repeat sequence ($ABCACB\cdots$) along

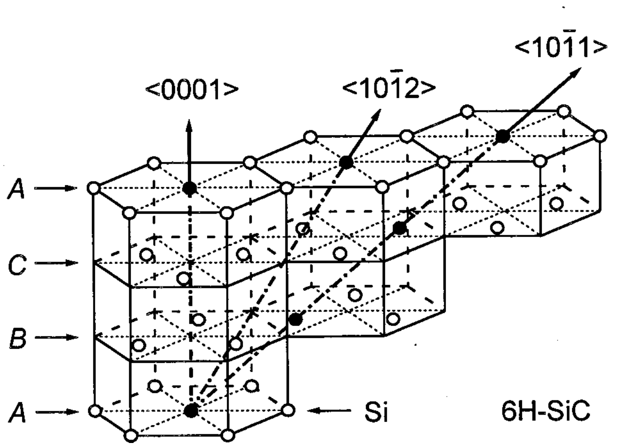

FIG. 1. First four Si layers (*ABCA*) of the crystallographic structure in 6*H*-SiC with the axes $\langle 0001\rangle$, $\langle 10\bar{1}2\rangle$, and $\langle 10\bar{1}1\rangle$ indicated. A complete six sequence of Si layers in 6*H*-SiC corresponds to *ABCACB* with carbon layers in-between.

the $\langle 0001\rangle$ axis that corresponds to a unit-cell height c of 1.5117 nm. The lattice parameter a is ~0.3081 nm and corresponds to the distance between neighboring Si or C atoms. Each carbon atom is positioned at the center of a Si tetrahedron, and the distance between the C atom and each of the Si atoms is ~0.1887 nm. The first four layers (*ABCA*) of Si atoms in the 6*H* stacking sequence are illustrated in Fig. 1. The lattice atoms are represented by circles, where the filled ones denote the on-axis Si atoms. The three crystallographic axes $\langle 0001\rangle$, $\langle 10\bar{1}2\rangle$, and $\langle 10\bar{1}1\rangle$ of interest in this study are also shown in the figure, which are situated in the same plane. The next two Si layers in the period are the mirror image of the layers *B* and *C* with respect to the top layer *A*. Carbon layers between each succeeding Si layers are not shown for the sake of clarity. The first carbon layer, located midway between the Si *A* and *B* layers, has the structure of the Si *C* layer, with all the Si atoms replaced by C atoms. The next five successive carbon layers resemble the Si layers *A*, *B*, *B*, *A*, and *C*, respectively. Note that from both crystallographic and channeling viewpoints, the $\langle 10\bar{1}2\rangle$ axis is completely equivalent to the $\langle 1\bar{1}02\rangle$ axis that was actually used in this study. Also, $\langle 0001\rangle$ and $\langle 10\bar{1}1\rangle$ axes in 6*H*-SiC correspond to $\langle 111\rangle$ and $\langle 100\rangle$, respectively, in the cubic structure of 3*C*-SiC ($ABCABC\cdots$ or $ACBACB\cdots$).

The lattice positions of six double layers of Si (filled circles) and C (open circles) atoms plus two double-layers belonging to the next period in 6*H*-SiC are illustrated along the $\langle 0001\rangle$, $\langle 10\bar{1}2\rangle$, and $\langle 10\bar{1}1\rangle$ axes in Fig. 2. Also shown are the relative orientations of the three axes. There is a horizontal shift to separate the Si and C layers for clarity. The $\langle 0001\rangle$ axis contains both Si and C atoms (mixed atomic rows) with an average atomic number $\bar{Z}_2$ of 10; both the $\langle 10\bar{1}2\rangle$ and $\langle 10\bar{1}1\rangle$ axes comprise either Si or C atoms (monoatomic rows), which make an angle α of 35.22° and 54.69°, respectively, with the $\langle 0001\rangle$ axis. The lattice atoms on the $\langle 0001\rangle$ axis are distributed uniformly with an interatomic spacing $\bar{d}$ equal to $c/4\,(0.3779\,\mathrm{nm})$, while the interatomic spacing along the $\langle 1\bar{1}02\rangle$ and $\langle 10\bar{1}1\rangle$ axes of either Si or C sublattice has an average distance of 0.4626 and 0.6538 nm, respectively. The geometrical and atomic parameters α, $\bar{d}$, and $\bar{Z}_2$ along the three axes are summarized in Table I, which will be used for the evaluation of mean lattice displacement distance $\bar{d}_d$ in Sec. V.

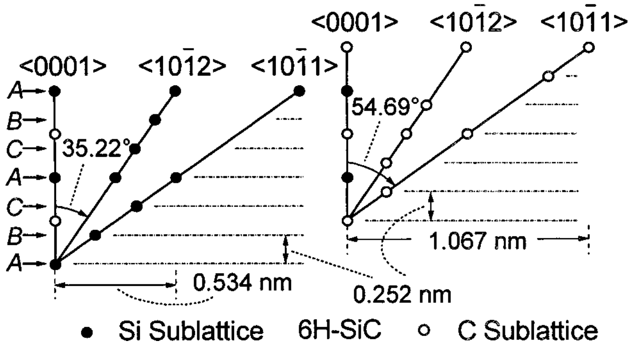

FIG. 2. Lattice sites of Si and C atoms in 6*H*-SiC along $\langle 0001\rangle$, $\langle 10\bar{1}2\rangle$, and $\langle 10\bar{1}1\rangle$ axes. The lattice constant a is 0.3081 nm, and the height of a unit cell c is 1.5117 nm.

III. EXPERIMENTAL PROCEDURE

A single crystal 6*H*-SiC wafer from Cree Research, Inc. was used in this study. The low value of the minimum yield ($\chi_{\mathrm{min}} \approx 3\%$) for the as-received sample confirms the excellent crystalline quality of the wafer. Both ion irradiation and ion-beam analysis were performed within the Environmental Molecular Sciences Laboratory at the Pacific Northwest National Laboratory.

In this study, three areas on the 6*H*-SiC wafer were irradiated at 300 K with 2 MeV Au^{2+} ions to fluences of 0.029, 0.058, and 0.12 ions/nm^2, respectively. The ion fluences were selected, based on previous 2 MeV Au^{2+} irradiation studies,[12,13] to produce relatively low damage levels along the $\langle 0001\rangle$ direction. A large tilt angle [60° off the (0001)-surface normal] was chosen to produce shallow damage that could be readily measured by *in situ* channeling methods. A low ion-beam flux of $\sim 10^{12}\mathrm{Au}^{2+}/\mathrm{cm}^2/\mathrm{sec}$ was utilized to avoid high-dose rate effects on damage production and to prevent significant beam heating during irradiation. A small irradiation area of $1.0\times 1.2\,\mathrm{mm}^2$ was used for each dose with a uniform beam intensity across the area (slit settings: $0.5\times 1.2\,\mathrm{mm}^2$). Subsequent to irradiation, *in situ* channeling analyses were performed using 0.94 MeV D^+ ions along

TABLE I. Axial angle (α) relative to $\langle 0001\rangle$ axis, average interatomic spacing ($\bar{d}$) and mean atomic number ($\bar{Z}_2$) along $\langle 0001\rangle$, $\langle 10\bar{1}2\rangle$, and $\langle 10\bar{1}1\rangle$ axes in 6*H*-SiC.

Axis	α (deg)	$\bar{d}$ (nm)	$\bar{Z}_2$	Comments
$\langle 0001\rangle$	0	0.3779	10	mixed Si and C rows
$\langle 10\bar{1}2\rangle$	35.22	0.4626	6 or 14	monoatomic rows
$\langle 10\bar{1}1\rangle$	54.69	0.6538	6 or 14	monoatomic rows

$\langle 0001 \rangle$, $\langle 1\bar{1}02 \rangle$, and $\langle 10\bar{1}\bar{1} \rangle$ axes. The analyzing beam ($0.5 \times 0.6\,\mathrm{mm}^2$) was collimated to an angular dispersion of less than 0.05° with a typical beam current of ~20 nA, which was centered in each irradiated area. The damage induced in the investigated depth region during the analysis was negligible according to experimental observations and SRIM-97 simulations.[35] Beam alignment to each of the chosen crystal directions was accurate to better than 0.05° by taking advantage of a precision manipulator on which the crystal wafer was mounted. The step-motor-driven manipulator, controlled by an end-station computer, provides two tilt axes (polar and flip) perpendicular to the beam direction and an azimuthal rotation axis, having an angular precision of 0.009°/step, 0.0005°/step, and 0.00044°/step, respectively. In addition, three linear translation stages x, y, and z integral with the manipulator were used for selection of separate spots on the target for study. A random-equivalent spectrum was obtained from the spectra that were recorded under various off-axis orientations with different combinations of polar and flip angles ranging from 3° to 7°. Angular scans around the $\langle 0001 \rangle$, $\langle 1\bar{1}02 \rangle$, and $\langle 10\bar{1}\bar{1} \rangle$ axes were also conducted with an increment of 0.1° in a range from $-2°$ to 2° along random to random direction. The intermittent action of sample rotation and data collection was fully controlled by the end-station computer using a self-developed code. The charge of the incident beam was accurately integrated by applying a high positive voltage (300 V) to the target in order to suppress the secondary electron emission from the target.

Simultaneous determination of disorder on both the Si and C sublattices in SiC was achieved based on the channeling geometry for $^{28}\mathrm{Si}(d,d)^{28}\mathrm{Si}$ RBS/C combined with $^{12}\mathrm{C}(d,p)^{13}\mathrm{C}$ NRA/C at a scattering or reaction angle of 150°. The low D^+ energy[12,27] (0.94 MeV) was selected to improve the depth resolution for profiling the narrow disorder distributions in the irradiated specimen. The energy stability of the incident D^+ ions was better than ± 3 keV, which is necessary to allow accurate analysis of the C sublattice from the (d,p) reaction. During both the ion irradiation and the channeling measurements, the vacuum in the target chamber was typically in the range of 10^{-6} Pa, and carbon contamination on the sample surface was not observed. *In situ* isochronal annealing experiments were also performed in vacuum at 570 K for 20 min. Similar ion-beam methods were employed to analyze the residual disorder in the annealed sample, and for these measurements, the channeling analysis was performed at room temperature to ensure that the recovery processes were quenched. Other experimental details, including the accelerator facility, target chamber and *in situ* temperature control systems have been described elsewhere.[36–38]

IV. DATA ANALYSIS

Ion fluences have been converted to an equivalent dose D in units of displacements per atom (dpa) that is given by the formula[12]

$$D = [R(x)/N]\Phi, \tag{1}$$

where $R(x)$ is the local production rate of displaced atoms (displacements/ion/cm) at depth x, N is the atomic density of $6H$-SiC ($9.64 \times 10^{22}\,\mathrm{atoms/cm^3}$), and Φ is the ion fluence (ions/cm^2). The value of $R(x)$ is the total number of displaced atoms on both the Si and C sublattices, which has been calculated for Au ions using SRIM-97 full-cascade simulations[35] under the assumptions of a sample density of 3.21 g/cm^3 and threshold displacement energies of 20 and 35 eV for the C and Si sublattices, respectively.[16] The factor $R(x)/N$ for conversion from ion fluence ($\mathrm{Au}^{2+}/\mathrm{nm}^2$) to dose in dpa is 0.5915 at the damage peak ($x = 108\,\mathrm{nm}$) under the irradiation conditions of this study.

The relative disorder n_d on the Si (or C) sublattice as a function of depth x can be obtained from the RBS/C (or NRA/C) spectra using the expression

$$n_d = \frac{h(x) - \chi_R(x)}{1 - \chi_R(x)}, \tag{2}$$

where $h(x)$ is the yield ratio of the aligned spectrum from the damaged crystal to the random spectrum at depth x, and $\chi_R(x)$ is the random (or dechanneled) fraction at depth x. Note that the random fraction in an undamaged crystal is the yield ratio of the aligned virgin spectrum to the random spectrum; however, the introduction of irradiation-induced defects increases the random fraction with depth due to the angular dispersion of the incident beam caused by the presence of the defects; thus, more dechanneling events are produced from the on-axis atoms. A linear dechanneling approximation has been used for $\chi_R(x)$, and the effects[39] from complex types of defects on the dechanneling yields are assumed to be negligible. To minimize statistical errors, experimental spectra were smoothed using the averages of five adjacent points prior to analysis.

The conversion from ion energy (or channel number) to depth x for the Si sublattice was accomplished by

$$x = (kE_0 - E_1)/(kS_{\mathrm{in}}/\cos\theta_1 + S_{\mathrm{out}}/\cos\theta_2), \tag{3}$$

where k is the kinetic factor for Si, E_0 is the incident D^+ ion energy, and E_1 is the energy detected for the ions backscattered from Si at depth x. The parameters θ_1 and θ_2 are the angles between the sample normal and the direction of the incident beam and of the scattered particles, respectively. Equation (3) assumes that the ion stopping powers along the inward (S_{in}) and outward (S_{out}) paths are both constants. Also, a mean-energy approximation approach[39] was applied in determining the stopping powers. For the analysis of irradiated areas, random stopping powers from the SRIM-97 database[35] are adopted. From a similar energetic consideration for the $^{12}\mathrm{C}(d,p)^{13}\mathrm{C}$ reaction with an energy release of $Q = 2.723\,\mathrm{MeV}$, the depth scale for C sublattice can be obtained.

The relationship between the root-mean-square (r.m.s.) displacement $\overline{u_1}$ (nm) and the observed angular half-width $\Psi_{1/2}$ (degree) is given by the following expression:[40]

$$\Psi_{1/2} = 0.8 F_{\mathrm{RS}}\left(\frac{12\overline{u_1}}{a_{\mathrm{TF}}}\right)\Psi_1, \tag{4}$$

where $F_{\mathrm{RS}}(\xi)$ is the square root of the Molière string potential that has been tabulated by Barett.[41] The quantities a_{TF} (nm) and Ψ_1 (degree) are the Thomas-Fermi screening radius and the Lindhard critical angle for channeling, respectively. The analytical forms for a_{TF} and Ψ_1 are given by

$$a_{\mathrm{TF}}=\frac{0.04685}{(Z_1^{1/2}+\overline{Z}_2^{1/2})^{2/3}} \tag{5}$$

and

$$\Psi_1=0.0971\left(\frac{Z_1\overline{Z}_2}{E_0\overline{d}}\right)^{1/2}, \tag{6}$$

where Z_1 and $\overline{Z}_2$ denote the atomic number of the projectile and the average atomic number of the host atoms on the axis, respectively; E_0 is the incident ion energy in MeV and $\overline{d}$ (nm) is the mean interatomic spacing along the axial direction.

The r.m.s. displacement $\overline{u_1}$ can be approximated by the r.m.s. thermal vibration amplitude u_1 for the atoms not displaced in a perfect crystal. It can also be determined from the r.m.s. thermal vibration amplitude and the mean lattice displacement distance $\overline{d_d}$ in a damage region by the relationship[30,31]

$$\overline{u_1}=\sqrt{(1-\overline{f_d})u_1^2+\overline{f_d}\overline{d_d^2}}, \tag{7}$$

where $\overline{f_d}$ is the mean fraction of the displaced atoms over a chosen depth region. The displaced atoms from the atomic strings include slightly displaced atoms due to lattice stress, single-interstitial configurations, interstitial clusters consisting of two or more atoms, and randomly arranged atoms in amorphous domains.

V. RESULTS AND DISCUSSION

A. Depth profile of disorder

In situ $\langle 0001\rangle$-aligned spectra for $6H$-SiC irradiated at 300 K with 2 MeV Au^{2+} to three low fluences are shown in Fig. 3. Also included are random and $\langle 0001\rangle$-aligned spectra from a virgin area, which respectively define the upper and lower levels of the scattering yields from the amorphous and essentially defect-free SiC materials. From Fig. 3, the damage peaks on the Si sublattice for the irradiated specimens are readily resolved from the D^+RBS/C. Although the damage peaks on the C sublattice also appear in the RBS/C spectra, accurate analysis of C disorder is not straightforward because of the low C scattering yield and spectrum overlap. At higher energies (larger channel numbers), the dechanneling contributions from the $^{12}\mathrm{C}(d,p)^{13}\mathrm{C}$ NRA/C (multiplied by a factor of 4 in Fig. 3) appear in a background-free region; thus, the C disorder is completely resolvable from the RBS/C spectra. This condition allows simultaneous analysis of disorder on both the Si and C sublattices from one measurement.

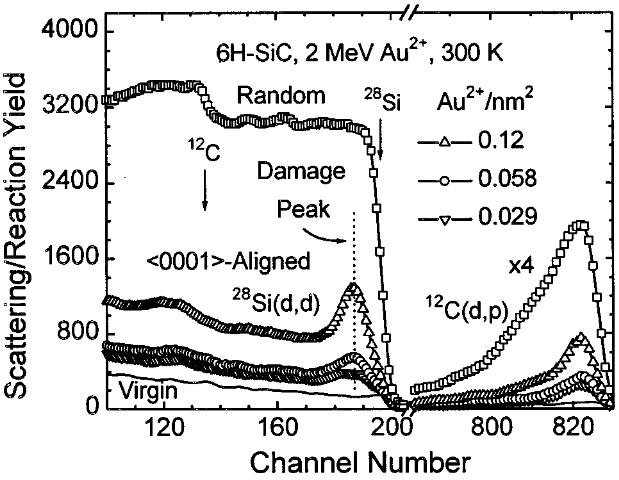

FIG. 3. *In situ* 0.94 MeV D^+ $\langle 0001\rangle$-aligned RBS/NRA spectra for $6H$-SiC irradiated with Au^{2+} at 300 K. Also included are random and channeling spectra from a virgin area.

The $\langle 0001\rangle$-, $\langle 1\overline{1}02\rangle$-, and $\langle 10\overline{1}1\rangle$-aligned RBS/NRA spectra for $6H$-SiC irradiated to 0.12 $\mathrm{Au}^{2+}/\mathrm{nm}^2$ at room temperature are shown in Fig. 4 for comparison. The slight channel shift of the damage peak is due to the different depth scales for the different orientations. Lower background dechanneling yields on both the Si and C sublattices are observed along the $\langle 0001\rangle$ axis than along the $\langle 1\overline{1}02\rangle$ and $\langle 10\overline{1}1\rangle$ axes. This is because there is a more open space accessible in the $\langle 0001\rangle$ channel that leads to a smaller probability for ions to be dechanneled and backscattered. In addition, although the normalized dechanneling yields just behind the damage peaks are the same on the Si and C sublattices along the $\langle 0001\rangle$ axis (0.25 vs 0.25), they are higher on the C sublattice along both the $\langle 1\overline{1}02\rangle$ and $\langle 10\overline{1}1\rangle$ axes (0.79 vs 0.65 and 0.69 vs 0.64, respectively). Similar results on the minimum yield $\chi_{\min}$ just behind the surface peak have been obtained from an unirradiated spot (data not

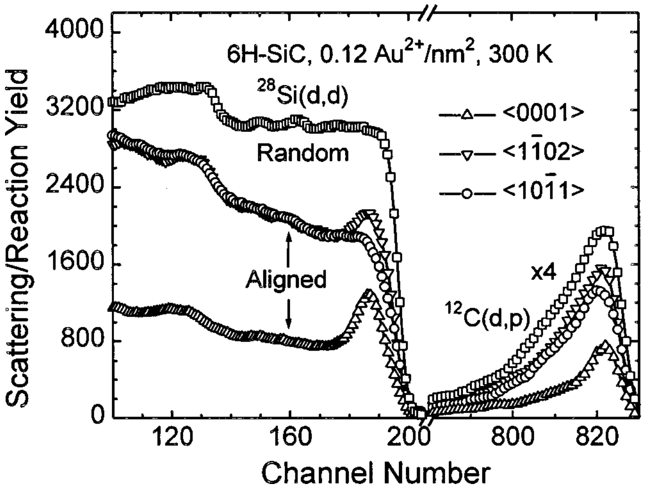

FIG. 4. *In situ* 0.94 MeV D^+ $\langle 0001\rangle$-, $\langle 1\overline{1}02\rangle$-, and $\langle 10\overline{1}1\rangle$-aligned RBS/NRA spectra for $6H$-SiC irradiated to 0.12 $\mathrm{Au}^{2+}/\mathrm{nm}^2$ at 300 K. Also included are random and channeling spectra from a virgin area.

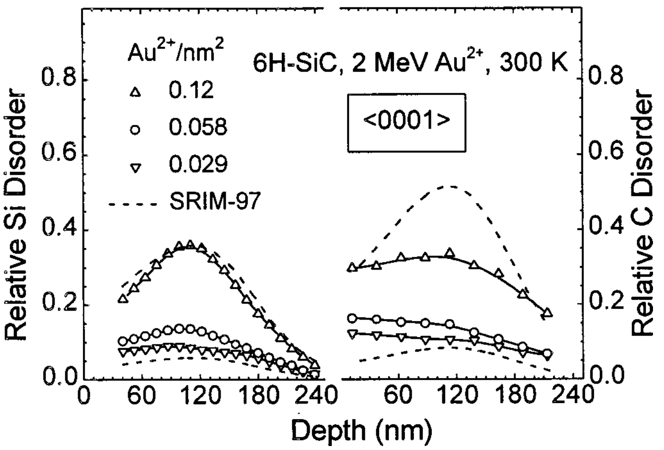

FIG. 5. Depth profiles of disorder on the Si and C sublattices in 6H-SiC irradiated to 0.029, 0.058, and 0.12 Au^{2+}/nm^2 at 300 K, observed along ⟨0001⟩ axis. Also included are the SRIM-97 results for 0.12 Au^{2+}/nm^2 (lower dashed line) and the results multiplied by a factor of 6.2 (upper dashed line) to match the height of the Si damage peak.

shown) of 6H-SiC, which is consistent with the behavior observed in virgin 3C-SiC.[42] This phenomenon is attributed to the separate monoatomic rows along the $\langle 1\bar{1}02\rangle$ and $\langle 10\bar{1}\bar{1}\rangle$ axes (Fig. 2 and Table I). According to Eq. (6), the C strings along the $\langle 1\bar{1}02\rangle$ or $\langle 10\bar{1}\bar{1}\rangle$ channel provide a smaller critical angle Ψ_1 for channeling than the Si strings; consequently, D^+ ions that can still be channeled along the Si strings, may jump to C strings where there is a higher probability for dechanneling because of the smaller critical angle (Ψ_1). Similar behavior of energetic ions channeled in a crystallographic plane has been well understood.[43] However, for ions initially channeled along the C strings, channeling along the Si strings is also possible because of larger Ψ_1. In spite of these jumping processes, the above data suggest that the dechanneling yield on the C sublattice is not significantly enhanced in the damage region along any of the directions.

The depth profiles of disorder analyzed along the ⟨0001⟩ axis for different irradiation doses are shown in Fig. 5. Full amorphization corresponds to a relative disorder of 1.0. The disorder profiles are determined from the results in Fig. 3 using Eq. (2) under the assumption of a linear dechanneling approximation for $\chi_R(x)$.[44] This procedure extracts the probability of close encounters between the energetic particles and the displaced atoms, which is directly proportional to the disorder concentration. The method gives the best evaluation of disorder concentration at and close to the damage peak, but brings about a slightly distorted depth profile on both sides.[44] However, the total number of displaced atoms can be evaluated to reasonable accuracy by integrating the entire damage profile despite the distortion. The depth scale in Fig. 5 has been converted based on Eq. (3), which is the distance from the surface along the normal direction (different geometry has been taken into account). It should be noted that due to sputtering processes, removal of Si and C atoms in the near-surface region might be a concern during the irradiation with heavy ions, such as Au^{2+}. Under the experimental conditions, SRIM-97 simulations indicate that the sputtering rate at the SiC surface corresponds to about 0.1 nm/(Au^{2+}/nm^2), assuming that the average surface binding energy is 6.05 eV (SRIM-97 default value) for both the Si and C sublattices. This low sputtering rate causes a removal of less than one atomic layer (0.012 nm) for the highest Au^{2+} fluence used in this study. Compared with the depth at the maximum damage (108 nm), as well as with the full width of the damage profiles (180 nm), the sputtering processes do not significantly affect the depth scale or the damage profiles at different ion fluences.

Also included in Fig. 5 are SRIM-97 results for comparison. The damage profiles and depth scale are in excellent agreement with the SRIM-97 simulation results. The simulated levels of relative disorder on both the Si and C sublattices produced at 0.12Au^{2+}/nm^2 (shown by a lower dashed line) are much lower than the respective experimental values. Such behavior suggests that the efficiency of disordering is higher than the displacement rate under these irradiation conditions, which is consistent with defect-stimulated disordering processes.[14] On the Si sublattice, the shape of the disorder profiles is quite consistent between the experiment results and the SRIM-97 full-cascade simulations for each ion fluence; an example for the highest dose is given in Fig. 5, where the simulated results are multiplied by a factor of 6.2 to match the height of the Si damage peak (shown by a upper dashed line). This suggests that the defect-stimulated disordering processes increase the Si disorder at a rate nearly proportional to the damage level. On the C sublattice, there is a larger discrepancy between experiment and simulation. At these low ion fluences, there is a notable distortion of the C disorder profiles characterized by disorder peaks that are flattened out and defect concentrations that are higher than expected in the near-surface region. The results may be attributed, in part, to C defect migration at 300 K, simultaneous in-cascade and dynamic defect recovery processes during irradiation, defect shielding by the ⟨0001⟩ atomic strings, and inadequacy of the linear dechanneling approximation for the NRA/C data.

The depth profiles of disorder on both the Si and C sublattices, as observed along the ⟨0001⟩, $\langle 1\bar{1}02\rangle$, and $\langle 10\bar{1}\bar{1}\rangle$ axes, are shown in Fig. 6 for 6H-SiC irradiated to 0.12 Au^{2+}/nm^2 at 300 K. The results indicate that the relative disorder on the C and Si sublattices, as observed along the ⟨0001⟩ axis, is of similar magnitude but much less than that observed along either the $\langle 1\bar{1}02\rangle$ or $\langle 10\bar{1}\bar{1}\rangle$ direction. Since exactly the same damage states exist during the measurements along each channeling direction, the results in Fig. 6 clearly suggest that a significant amount of disorder on the C and Si sublattices is shielded by the ⟨0001⟩ atomic strings. At this ion fluence, the relative shielding efficiency on the Si and C sublattices is largest for ⟨0001⟩ and decreases for $\langle 10\bar{1}\bar{1}\rangle$ and $\langle 1\bar{1}02\rangle$, respectively. At and below a fluence of 0.058Au^{2+}/nm^2, the shielding efficiency decreases in the order ⟨0001⟩, $\langle 1\bar{1}02\rangle$, $\langle 10\bar{1}\bar{1}\rangle$ (data not shown). The results in Fig. 6 also suggest that channeling analysis of disorder along the $\langle 1\bar{1}02\rangle$ or $\langle 10\bar{1}\bar{1}\rangle$ axis may be advantageous at low

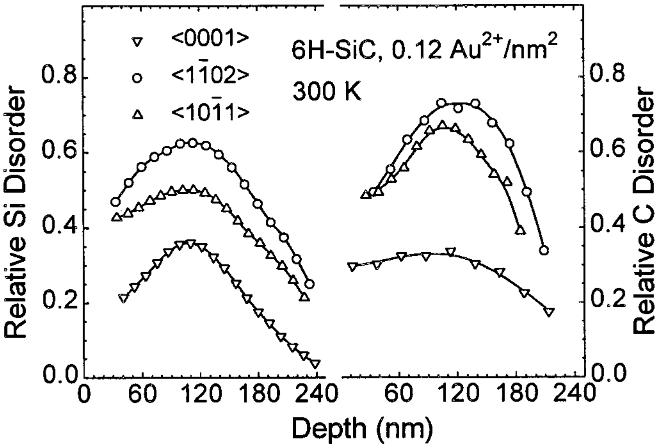

FIG. 6. Depth profiles of disorder on the Si and C sublattices in $6H$-SiC irradiated to 0.12 $\mathrm{Au}^{2+}/\mathrm{nm}^2$ at 300 K, observed along $\langle 0001\rangle$, $\langle 1\bar{1}02\rangle$, and $\langle 10\bar{1}1\rangle$ axes.

doses (low damage levels) because more types of defects or disorder induced by Au^{2+} in $6H$-SiC are probed by the incident beam, and thus can be analyzed. The $\langle 0001\rangle$-axial channeling, however, may be the best choice for the study of amorphization processes because the dechanneling yield along this axis is minimized and any amorphous domains and/or large clusters in the crystal structure should be revealed more clearly. For the same reason, the $\langle 0001\rangle$ axial channeling is also more suitable to use in studying high damage levels and for determining the dose for complete amorphization.[7,12,13,27]

B. Disorder accumulation

The accumulated disorder (n_d) at the damage peak for both the Si and C sublattices, observed along $\langle 0001\rangle$, $\langle 1\bar{1}02\rangle$, and $\langle 10\bar{1}1\rangle$ axes is shown in Fig. 7 as a function of dose in dpa [converted from ion fluence using Eq. (1)]. In general, the accumulated disorder shows a strong orientation dependence at the low doses, as has been observed for the highest dose in Fig. 6. While damage accumulation is linear along $\langle 0001\rangle$ in this dose regime, it is significantly larger and sublinear along both $\langle 1\bar{1}02\rangle$ and $\langle 10\bar{1}1\rangle$. The results for the $\langle 0001\rangle$ axis in Fig. 7 are quantitatively consistent with the published data[12] for $6H$-SiC irradiated at room temperature with Au^{2+} over a full range of damage levels. A lower level of disorder on both sublattices is observed along the $\langle 0001\rangle$ axis than along the other two axes studied. This result is consistent with previous results[7,33] for $6H$-SiC irradiated at 300 K with Ar^{2+} ions, where a lower level of disorder on the Si sublattice was observed along the $\langle 0001\rangle$ channel than along the $\langle 1\bar{1}02\rangle$ channel. Similar results have also been reported for B^{+}-implanted Si, where a lower concentration of Si disorder is observed[45] along the $\langle 111\rangle$ axis (equivalent to the $\langle 0001\rangle$ axis in the hexagonal structure of $6H$-SiC). Since amorphous domains or larger three-dimensional defect clusters should be equally observable along all channeling directions, the results in Fig. 7 suggest that some interstitial defect types in SiC are well aligned with the $\langle 0001\rangle$ axis or shielded along $\langle 0001\rangle$ by the stacking arrangements. This behavior may be associated with shielded interstitial configurations, such as the split interstitial (dumbbell) defects that are the most stable interstitial configurations in $3C$-SiC according to recent *ab initio* calculations.[46]

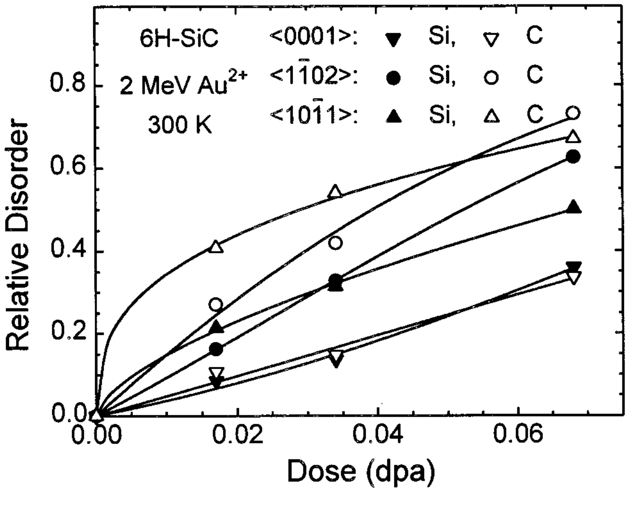

FIG. 7. Relative disorder on the Si and C sublattices, observed along $\langle 0001\rangle$, $\langle 1\bar{1}02\rangle$, and $\langle 10\bar{1}1\rangle$ axes, as a function of dose in displacement per atom (dpa) at the damage peak in $6H$-SiC irradiated with Au^{2+} at 300 K.

The results in Fig. 7 also show that a higher level of disorder is observed on the C sublattice than on the Si sublattice along the $\langle 1\bar{1}02\rangle$ and $\langle 10\bar{1}1\rangle$ axes, and a comparable level of disorder on both sublattices is observed along the $\langle 0001\rangle$ axis. These results suggest that more C defects than Si defects are shielded by the $\langle 0001\rangle$ atomic rows. The higher C disorder observed along $\langle 1\bar{1}02\rangle$ and $\langle 10\bar{1}1\rangle$ is attributed to a smaller threshold displacement energy on the C sublattice, which is consistent with molecular dynamics (MD) simulations[15–21] and other experimental measurements.[47] It is worth noting that although the results do not completely overlap the corresponding curves at the damage peak (Fig. 7), the accumulation of disorder in the near-surface regime (~50 nm) and over the entire damage region (data not shown) shows similar behavior of interstitial shielding by the $\langle 0001\rangle$ atomic strings and a higher level of C disorder along $\langle 1\bar{1}02\rangle$ and $\langle 10\bar{1}1\rangle$ axes.

From previous thermal annealing studies,[11–13,27] it is known that both single-interstitial configurations and large defect clusters are simultaneously produced in Au^{2+}-irradiated $6H$-SiC. In recent MD simulations,[19] it has been found that besides the efficient production of dispersed single interstitials (and vacancies), a few larger three-dimensional defect clusters containing up to 35 interstitials are produced in a single subcascade by Au projectiles in $3C$-SiC. In these MD simulations of Au cascades,[19] the largest clusters are amorphous in character, and the ratio of the interstitial clusters containing two or more interstitials to the total number of interstitials is 0.53. The types and distributions of the irradiation-induced defects in $6H$-SiC are believed to be similar to those in $3C$-SiC because the local

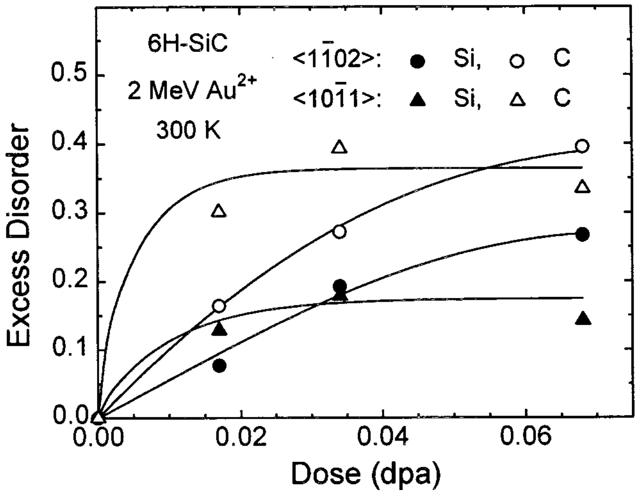

FIG. 8. Relative disorder along $\langle 1\bar{1}02\rangle$ and $\langle 10\bar{1}1\rangle$ subtracted from the disorder along $\langle 0001\rangle$ as a function of dose (dpa) at the damage peak in 6H-SiC irradiated with Au^{2+} at 300 K.

tetragonal structure is identical for all SiC polytypes. From the results in Fig. 7, the ratio of the total relative disorder (fraction of the displaced Si and C atoms) along $\langle 0001\rangle$ to that along $\langle 1\bar{1}02\rangle$ and $\langle 10\bar{1}1\rangle$ ranges from 0.31 at 0.017 dpa to 0.59 at 0.068 dpa, which is consistent with the ratio of interstitials in clusters to the total number of interstitials. Since large interstitial clusters and amorphous domains should be equally observable along all the three directions, these results, taken in light of the MD simulation results, suggest that the primary disorder observed along the $\langle 0001\rangle$ axis may be in the form of large interstitial or amorphous clusters. Likewise, the results suggest that a majority of the irradiation-induced single interstitials may be shielded by the on-axis atoms along $\langle 0001\rangle$. While this interpretation may be consistent with the MD simulations[19] and with the stable interstitial configurations predicted by *ab initio* calculations,[46] it should be considered as only speculative. More work will be required to confirm this interpretation.

The excess disorder observed along the $\langle 1\bar{1}02\rangle$ and $\langle 10\bar{1}1\rangle$ directions relative to that observed along $\langle 0001\rangle$ is obtained by subtracting the $\langle 0001\rangle$ results in Fig. 7 from the other results. This excess disorder is shown in Fig. 8 as a function of dose at the damage peak. The solid lines are the data fits using a damage ingrowth model for defect accumulation.[48] The relative excess disorder excludes the contribution of three-dimensional interstitial and amorphous clusters that are observable along all axes; thus the results in Fig. 8 should be largely representative of the stable single-interstitial concentrations along each respective axis. The results in Fig. 8 indicate that the unshielded Si and C interstitials along $\langle 10\bar{1}1\rangle$ tend to saturate at ~0.02 dpa, while those along $\langle 1\bar{1}02\rangle$ show a slower approach to saturation. The result suggests that the dose for the saturation of unshielded interstitial concentrations is orientation dependent. Above the saturation dose, cascade overlap and cluster coalescence may occur, as observed in recent MD simulations.[22] For 6H-SiC irradiated with Au^{2+} to low fluences at 300 K, the dose needed to achieve interstitial saturation along $\langle 1\bar{1}02\rangle$ is higher than that along $\langle 10\bar{1}1\rangle$.

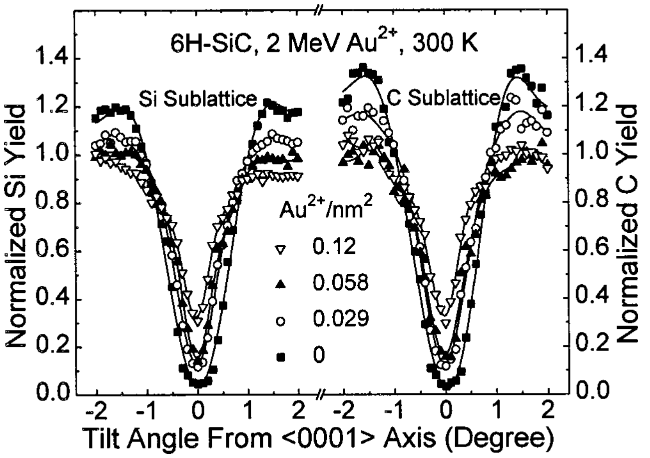

FIG. 9. Angular dependence of the normalized scattering yield around $\langle 0001\rangle$ axis in 6H-SiC irradiated with Au^{2+} to low doses at 300 K. Also included are the profiles from an unirradiated area.

C. Lattice displacement distance

The angular yield profiles around the $\langle 0001\rangle$ axis in 6H-SiC irradiated to the three low fluences at 300 K is shown in Fig. 9. Also included in the figure are the dip curves from an unirradiated area. To achieve better statistics without introducing significant damage from the analyzing beam, the yield integration in Fig. 9 was performed over a depth region from 30 to 220 nm, corresponding to channel numbers 177–194 for Si and 817–827 for C, where the damage profiles were located. As expected, the normalized yield increases and the angular half-width $\Psi_{1/2}$ decreases with increasing dose. Angular profiles around the other two axes (data not shown) exhibit similar behavior.

The angular yield curves for the Si and C sublattices around $\langle 0001\rangle$, $\langle 1\bar{1}02\rangle$, and $\langle 10\bar{1}1\rangle$ axes in 6H-SiC irradiated to a fluence of $0.058\mathrm{Au}^{2+}/\mathrm{nm}^2$ at 300 K are shown in Fig. 10. Clearly, the angular profiles for the Si and C atoms around the $\langle 0001\rangle$ axis completely overlap at both unirradiated and irradiated spots. This is because along the mixed atomic rows of the $\langle 0001\rangle$ axis (Fig. 2), ions experience an average potential created by the Si and C atoms on the axis, resulting in the same angular width ($\Psi_{1/2}$) for the Si and C sublattices. In contrast, the C angular profiles around both the $\langle 1\bar{1}02\rangle$ and $\langle 10\bar{1}1\rangle$ axes show a smaller $\Psi_{1/2}$ because of the smaller atomic number on the C strings along the axes. This merit is often applied to identify the exact substitutional location of implanted species in crystal structures.[49] Similar features of angular profiles (not shown) for other doses were also observed.

Based on the angular profiles (Figs. 9 and 10 and other data not shown), the half-widths $\Psi_{1/2}$ have been evaluated for both the Si and C sublattices, and the results are given in Table II. Since $\Psi_{1/2}$ is closely associated with the mean lattice displacement distance $\bar{d}_d$ from the atomic rows, the

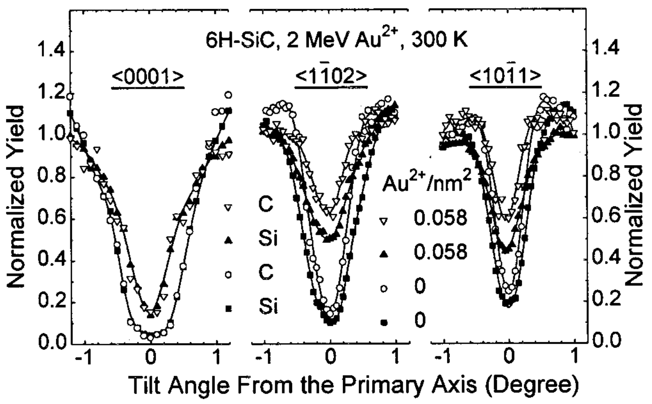

FIG. 10. Angular dependence of the normalized scattering yield around ⟨0001⟩, ⟨$1\bar{1}02$⟩, and ⟨$10\bar{1}\bar{1}$⟩ axes in $6H$-SiC irradiated with Au^{2+} at 300 K. Also included are the profiles from an unirradiated area.

change in $\Psi_{1/2}$ values reflects the degree of lattice distortion. From Table II, the half-width decreases monotonically with increasing ion fluence along all the axes studied. From Eqs. (4)–(6) and Table I, the root-mean-square (r.m.s) displacements $\overline{u_1}$ have been evaluated and are included in Table II. Comparable values of $\overline{u_1}$ are found for the Si and C sublattices along each axis at each ion fluence, except for the C sublattice along the ⟨$1\bar{1}02$⟩ axis, where the deviation at the highest dose might be caused by a large experimental error of $\Psi_{1/2}$. The r.m.s displacement at zero dose (from an unirradiated spot) represents the thermal vibration amplitude for the unirradiated crystal and is generally smaller than that in the damage region, as expected.

The mean fraction of displaced atoms $\overline{f_d}$ over the damage region (30–220 nm) is assumed to be the average disorder concentration $\overline{n_d}$ over the same damage region as for the angular profiles (from 30 to 220 nm) and is given in Table II. Since the as-received $6H$-SiC wafer had a high crystalline quality ($\chi_{\min}\approx 3\%$ on Si along ⟨0001⟩), zero displacement is assumed for both the Si and C sublattices in the $6H$-SiC crystal prior to irradiation. The disorder in the Au^{2+}-induced damage layer includes all types of defects, clusters and amorphous domains that may be formed by damage cascades.[19,22]

The mean lattice displacement distance $\overline{d_d}$ perpendicular to each respective axis, is evaluated using Eq. (7) and the results are summarized in Table II. This distance contains the contributions from not only stable single-interstitials and interstitial clusters, but also the slightly displaced atoms due to lattice distortion.[30,31,50] In general, the $\overline{d_d}$ values in Table II are comparable for the Si and C sublattices under the irradiation conditions, except for the C sublattice along the ⟨$1\bar{1}02$⟩ axis where a larger experimental error of the $\Psi_{1/2}$ might have occurred at the highest dose. The mean lattice displacement distance from the ⟨0001⟩, ⟨$1\bar{1}02$⟩, and ⟨$10\bar{1}\bar{1}$⟩ axes ranges from 0.014 to 0.037 nm in the applied dose region. Comparable and larger values also have been determined in low-dose Se$^+$ irradiated InP (Ref. 31) and GaAs (Ref. 30) single crystals, respectively. From Table II, there is a steady increase in $\overline{d_d}$ with ion fluence from the ⟨$10\bar{1}\bar{1}$⟩-axial observation, while an increase followed by a decrease in $\overline{d_d}$, is observed along the ⟨0001⟩ axis. These results may be qualitatively interpreted based on the lattice stress.[30,31] At very low fluences, isolated defects can cause a remarkable lattice stress field. As a result, a larger number of small atomic displacements surrounding the defects are pro-

TABLE II. Angular half-width ($\Psi_{1/2}$), root-mean-square displacement ($\overline{u_1}$), mean fraction of displaced atoms ($\overline{f_d}$), and mean lattice displacement distance ($\overline{d_d}$) perpendicular to each corresponding axis in $6H$-SiC irradiated at 300 K.

Fluence	$\Psi_{1/2}$ (deg)		$\overline{u_1}$ (nm)		$\overline{f_d}$		$\overline{d_d}$ (nm)	
(Au^{2+}/nm^2)	Si	C	Si	C	Si	C	Si	C
⟨0001⟩								
0	0.600	0.595	0.0026	0.0026	0	0	0	0
0.029	0.475	0.475	0.0060	0.0060	0.0644	0.0994	0.022	0.017
0.058	0.420	0.430	0.0086	0.0081	0.0915	0.1290	0.027	0.022
0.12	0.395	0.385	0.0102	0.0109	0.2295	0.2855	0.021	0.020
⟨$1\bar{1}02$⟩								
0	0.390	0.290	0.0113	0.0102	0	0	0	0
0.029	0.370	0.260	0.0126	0.0134	0.1304	0.2117	0.019	0.022
0.058	0.355	0.250	0.0140	0.0146	0.2660	0.3452	0.020	0.021
0.12	0.350	0.205	0.0144	0.0223	0.5068	0.6072	0.017	0.027
⟨$10\bar{1}\bar{1}$⟩								
0	0.295	0.220	0.0144	0.0133	0	0	0	0
0.029	0.295	0.210	0.0144	0.0146	0.1926	0.3732	0.014	0.017
0.058	0.280	0.200	0.0160	0.0163	0.2623	0.4415	0.020	0.019
0.12	0.215	0.150	0.0261	0.0288	0.4140	0.5652	0.037	0.037

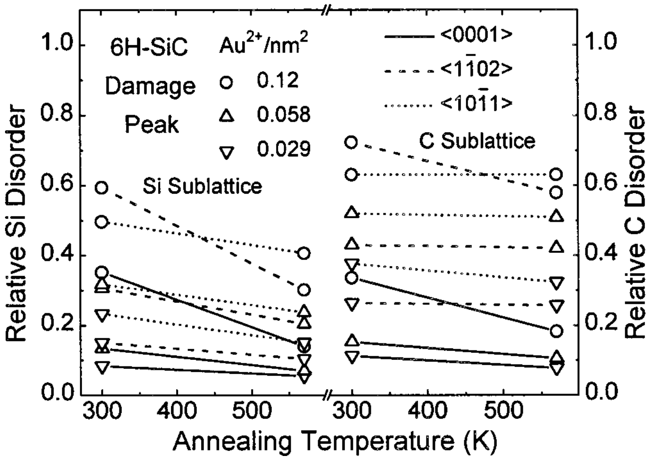

FIG. 11. Thermal recovery (20 min) of relative disorder on the Si and C sublattices at the damage peak, observed along $\langle 0001\rangle$, $\langle 1\bar{1}02\rangle$, and $\langle 10\bar{1}1\rangle$ axes, in Au^{2+}-irradiated $6H$-SiC as a function of annealing temperature.

duced. During the stage of the small-displacement accumulation, the mean lattice displacement distance increases with increasing ion fluence. This is what is observed along the $\langle 10\bar{1}1\rangle$ axis. With further increase of ion fluence, defect clustering can occur, which can efficiently reduce the lattice stress. A reduction of the lattice stress is expected to result in a decrease in the mean lattice displacement distance. This may explain the change of the values in $\overline{d}_d$ perpendicular to the $\langle 0001\rangle$ axis. The data further suggest that an observable reduction of the lattice stress occurs at a fluence of 0.12 $\mathrm{Au}^{2+}/\mathrm{nm}^2$.

It may be worthwhile to mention that in combination with computer simulations, the lattice displacement distance can be more accurately determined (to within 0.02 Å).[50,51] Several research groups have recently applied a Monte Carlo method[52] to simulate the angular profiles of implanted species and determine their lattice displacement distance from the atomic rows.[28,29] This method may also provide an effective means for accurate determination of the lattice displacement distance of host lattice atoms. Further analysis of the current data and any additional new data will be performed using the computer simulations, and the results will be reported at a later date.

D. Disorder recovery

The general behavior of disorder recovery in Au^{2+} irradiated $6H$-SiC observed along $\langle 0001\rangle$ axis, has been reported.[12,13] Since there are considerable shielding effects of the $\langle 0001\rangle$ atomic rows on some types of irradiation-induced defects as discussed above, studies of defect recovery along other axes might lead to some important insights. For this reason, thermal annealing of the irradiated sample was performed and multiaxial channeling analysis of the residual disorder at each ion fluence was measured.

The isochronal annealing results at 570 K are shown in Fig. 11. Similar recovery behavior is observed on the Si and C sublattices along the three chosen axes. Previous $\langle 0001\rangle$-axial channeling studies for $6H$-SiC irradiated with Au^{2+} and He^{+} ions up to much higher doses also indicated similar recovery process on both the Si and C sublattices.[12,13,27] The results in Fig. 11 indicate that there is only a moderate recovery of disorder at low ion fluences (at and below 0.058 $\mathrm{Au}^{2+}/\mathrm{nm}^2$) along each of the directions, which may be associated, in part, with the presence of defect clusters and/or amorphous zones formed during Au^{2+}-irradiation at 300 K, as discussed above. More significant recovery is observed for 0.12 $\mathrm{Au}^{2+}/\mathrm{nm}^2$ along both the $\langle 0001\rangle$ and $\langle 1\bar{1}02\rangle$ axes, but is not observed along the $\langle 10\bar{1}1\rangle$ axis, indicating that most of the recovered defects were well shielded by the atomic strings along the $\langle 10\bar{1}1\rangle$ axis (equivalent to the $\langle 100\rangle$ axis in $3C$-SiC) and that recovery processes for these defects appear to be coupled to disorder observed along $\langle 0001\rangle$ and $\langle 1\bar{1}02\rangle$. These defects may be in the form of single interstitials, planar interstitial defects (dislocations) as observed by transmission electron microscopy (TEM),[53] the split interstitial (dumbbell) defects predicted by *ab initio* results,[46] and/or other types of defects that were aligned with the $\langle 10\bar{1}1\rangle$ axis. Since the ion-channeling method does not generally identify the defect types present in crystals, complementary studies using computer simulations and TEM methods are necessary to determine the nature of the defects and the related dynamic and kinetic processes in $6H$-SiC.

VI. CONCLUSIONS

Damage accumulation and recovery in Au^{2+} irradiated $6H$-SiC have been studied using D^{+} channeling along $\langle 0001\rangle$, $\langle 1\bar{1}02\rangle$, and $\langle 10\bar{1}1\rangle$ axes. At and below 0.12 $\mathrm{Au}^{2+}/\mathrm{nm}^2$, a similar level of low disorder on both the Si and C sublattices is observed along the $\langle 0001\rangle$ axis. Higher levels of disorder and more C defects than Si defects are observed along the $\langle 1\bar{1}02\rangle$ and $\langle 10\bar{1}1\rangle$ directions. The results suggest that some of the Si and C defects are well aligned with the $\langle 0001\rangle$ axis. Furthermore, more C defects than Si defects are shielded by the $\langle 0001\rangle$ atomic rows than the $\langle 1\bar{1}02\rangle$ and $\langle 10\bar{1}1\rangle$ atomic rows. These shielded defects may include single interstitials and split interstitial defects. The higher C disorder at low doses is consistent with MD simulations[15–21] and other experimental data[47] that suggest a smaller threshold displacement energy on the C sublattice. A similar behavior of disorder accumulation at the damage peak, in the near-surface regime and over the entire damage region is observed under these low ion fluences. The mean lattice displacement distance perpendicular to the $\langle 0001\rangle$, $\langle 1\bar{1}02\rangle$, and $\langle 10\bar{1}1\rangle$ axes, determined by the angular half-width and mean fraction of displaced atoms, ranges from 0.014 to 0.037 nm and shows comparable values for the Si and C sublattices. A steady accumulation of small lattice displacements due to lattice stress is observed along the $\langle 10\bar{1}1\rangle$ axis, and a detectable reduction of the lattice stress perpendicular to the $\langle 0001\rangle$ axis occurs at 0.12 $\mathrm{Au}^{2+}/\mathrm{nm}^2$. There is only a moderate amount of thermal recovery of disorder at 570 K at low ion fluences (at and below 0.058 $\mathrm{Au}^{2+}/\mathrm{nm}^2$) in $6H$-SiC. The apparent recovery at 0.12 Au^{2+}/nm^2, as observed along both the $\langle 0001\rangle$ and $\langle 1\bar{1}02\rangle$ directions, but barely along the $\langle 10\bar{1}1\rangle$ directions, indicates that a majority of the recovered defects in the thermal annealing process (570 K, 20 min) are shielded by the $\langle 10\bar{1}1\rangle$ atomic strings in 6*H*-SiC.

ACKNOWLEDGMENTS

This research was supported by the Division of Materials Sciences and Engineering, Office of Basic Energy Sciences, U.S. Department of Energy. Support for the accelerator facilities within the Environmental Molecular Sciences Laboratory (EMSL) was provided by the Office of Biological and Environmental Research, U.S. Department of Energy. The Pacific Northwest National Laboratory is operated by Battelle Memorial Institute for the U.S. Department of Energy under Contract No DE-AC 06-76RLO 1830. The authors are grateful to S. Thevuthasan and V. Shutthanandan for their technical assistance with accelerator operations during ion irradiation and ion-beam analysis and to F. Gao for helpful discussions.

---

[*] Author to whom correspondence should be addressed: Pacific Northwest National Laboratory, MSIN K8-93, P.O. Box 999, Richland, WA 99352; Email address: Weilin.Jiang@pnl.gov

[1] R. F. Davis, *Proceedings of the International Conference on SiC and Related Materials*, Institute of Physics Publishing Conference Series No. **137** (IOP, Publishing, London, 1994), p. 1.

[2] C. G. Masi, R&D (Cahners) **July**, 14 (2000).

[3] C. Raynaud, J. Non-Cryst. Solids **280**, 1 (2001).

[4] P. Fenici, A. J. Frias Rebelo, R. H. Jones, A. Kohyama, and L. L. Snead, J. Nucl. Mater. **258–263**, 215 (1998).

[5] B. G. Kim, Y. Choi, J. W. Lee, Y. W. Lee, D. S. Sohn, and G. M. Kim, J. Nucl. Mater. **281**, 163 (2000).

[6] R. A. Verrall, M. D. Vlajic, and V. D. Krstic, J. Nucl. Mater. **274**, 54 (1999).

[7] W. J. Weber, L. M. Wang, N. Yu, and N. J. Hess, Mater. Sci. Eng., A **253**, 62 (1998).

[8] E. Wendler, A. Heft, and W. Wesch, Nucl. Instrum. Methods Phys. Res. B **141**, 105 (1998).

[9] S. J. Zinkle and L. L. Snead, Nucl. Instrum. Methods Phys. Res. B **116**, 92 (1996).

[10] C. J. McHargue and J. M. Williams, Nucl. Instrum. Methods Phys. Res. B **80–81**, 889 (1993).

[11] W. J. Weber, W. Jiang, and S. Thevuthasan, Nucl. Instrum. Methods Phys. Res. B **166–167**, 410 (2000).

[12] W. Jiang, W. J. Weber, S. Thevuthasan, and V. Shutthanandan, J. Nucl. Mater. **289**, 96 (2001).

[13] W. J. Weber, W. Jiang, and S. Thevuthasan, Nucl. Instrum. Methods Phys. Res. B **175–177**, 26 (2001).

[14] W. J. Weber, Nucl. Instrum. Methods Phys. Res. B **166–167**, 98 (2000).

[15] R. Devanathan, W. J. Weber, and T. Diaz de la Rubia, Nucl. Instrum. Methods Phys. Res. B **141**, 118 (1998).

[16] R. Devanathan and W. J. Weber, J. Nucl. Mater. **278**, 258 (2000).

[17] J. M. Perlado, L. Malerba, A. Sanchez-Rubio, and T. Diaz de la Rubia, J. Nucl. Mater. **276**, 235 (2000).

[18] F. Gao and W. J. Weber, Phys. Rev. B **63**, 054101 (2000).

[19] F. Gao and W. J. Weber, J. Appl. Phys. **89**, 4275 (2001).

[20] L. Malerba, J. M. Perlado, A. Sanchez-Rubio, I. Pastor, L. Colombo, and T. Diaz de la Rubia, J. Nucl. Mater. **283–287**, 794 (2000).

[21] L. Malerba and J. M. Perlado, J. Nucl. Mater. **289**, 57 (2001).

[22] F. Gao and W. J. Weber, Mat. Res. Soc. Symp. Proc. **650**, R3.20.1 (2001).

[23] W. Jiang, W. J. Weber, S. Thevuthasan, and R. Grötzschel, Nucl. Instrum. Methods Phys. Res. B **166–167**, 374 (2000).

[24] W. Jiang, W. J. Weber, S. Thevuthasan, and D. E. McCready, Nucl. Instrum. Methods Phys. Res. B **148**, 557 (1999).

[25] W. Jiang, W. J. Weber, and S. Thevuthasan, Mat. Res. Symp. Proc. **540**, 183 (1999).

[26] W. Jiang, W. J. Weber, S. Thevuthasan, and D. E. McCready, J. Nucl. Mater. **257**, 295 (1998).

[27] W. Jiang, W. J. Weber, S. Thevuthasan, and R. Grötzschel, Nucl. Instrum. Methods Phys. Res. B **161–163**, 501 (2000).

[28] E. Alves, M. F. da Silva, J. G. Marques, J. C. Soares, and K. Freitag, Mater. Sci. Eng., B **59**, 207 (1999).

[29] A. Seppälä, R. Salonen, J. Slotte, T. Ahlgren, E. Rauhala, and J. Räisänen, Nucl. Instrum. Methods Phys. Res. B **161–163**, 520 (2000).

[30] E. Wendler, F. Schrempel, P. Müller, K. Gärtner, and W. Wesch, Nucl. Instrum. Methods Phys. Res. B **118**, 367 (1996).

[31] F. Schrempel, T. Opfermann, E. Wendler, and W. Wesch, Nucl. Instrum. Methods Phys. Res. B **161–163**, 515 (2000).

[32] J. A. Edmond, R. F. Davis, S. P. Withrow, and K. L. More, J. Mater. Res. **3**, 321 (1988).

[33] W. J. Weber, N. Yu, and L. M. Wang, J. Nucl. Mater. **253**, 53 (1998).

[34] W. J. Weber and N. Yu, Nucl. Instrum. Methods Phys. Res. B **127–128**, 191 (1997).

[35] J. F. Ziegler, J. P. Biersack, and U. Littmark, *The Stopping and Range of Ions in Solids* (Pergamon, New York, 1985).

[36] S. Thevuthasan, C. H. F. Peden, M. H. Engelhard, D. R. Baer, G. S. Herman, W. Jiang, Y. Liang, and W. J. Weber, Nucl. Instrum. Methods Phys. Res. A **420**, 81 (1999).

[37] W. Jiang, W. J. Weber, and S. Thevuthasan, J. Appl. Phys. **87**, 7671 (2000).

[38] W. Jiang, W. J. Weber, S. Thevuthasan, and D. E. McCready, Surf. Interface Anal. **27**, 179 (1999).

[39] W. K. Chu, J. W. Mayer, and M. A. Nicolet, *Backscattering Spectrometry* (Academic, New York, 1978).

[40] *Ion Beam Handbook for Material Analysis*, edited by J. W. Mayer and E. Rimini (Academic, New York, 1977), p. 69.

[41] J. H. Barett, Phys. Rev. B **3**, 1527 (1971).

[42] I. Nashiyama, T. Nishijima, E. Sakuma, S. Yoshida, Nucl. Instrum. Methods Phys. Res. B **33**, 599 (1988).

[43] *Channeling: Theory, Observation and Applications*, edited by D. V. Morgan (Wiley, London, 1973), p. 53.

[44] *Handbook of Modern Ion Beam Materials Analysis*, edited by J. R. Tesmer and M. Nastasi (Materials Research Society, Pittsburgh, PA, 1995), p. 267.

[45] B. Weber, E. Wendler, K. Gärtner, D. M. Stock, and W. Wesch, Nucl. Instrum. Methods Phys. Res. B **118**, 113 (1996).

[46] F. Gao, E. J. Bylaska, W. J. Weber, and L. R. Corrales, Phys. Rev. B (to be published).

[47] S. J. Zinkle and C. Kinoshita, J. Nucl. Mater. **251**, 200 (1997).

[48] W. J. Weber, J. Nucl. Mater. **98**, 206 (1981).

[49] H. Kobayashi and W. M. Gibson, Appl. Phys. Lett. **73**, 1406 (1998).

[50] W. Wesch, A. Jordanov, K. Gärtner, and G. Götz, Nucl. Instrum. Methods Phys. Res. B **39**, 445 (1989).

[51] K. Gärtner, K. Hehl, and G. Schlotzhauer, Nucl. Instrum. Methods Phys. Res. B **4**, 55 (1984).

[52] P. J. M. Smulders and D. O. Boerma, Nucl. Instrum. Methods Phys. Res. B **29**, 471 (1987).

[53] P. O. Å. Persson, W. Skorupa, D. Panknin, A. Kuznetsov, A. Hallén, and L. Hultman, Mat. Res. Soc. Symp. Proc. **640**, H6.2.1 (2001).